



**HAL**  
open science

# Rain gauge networks' limitations and the implications to hydrological modelling highlighted with a X-band radar

Igor Paz, Ioulia Tchiguirinskaia, Daniel Schertzer

## ► To cite this version:

Igor Paz, Ioulia Tchiguirinskaia, Daniel Schertzer. Rain gauge networks' limitations and the implications to hydrological modelling highlighted with a X-band radar. *Journal of Hydrology*, 2020, 583, pp.124615 -. 10.1016/j.jhydrol.2020.124615 . hal-03489546

**HAL Id: hal-03489546**

**<https://hal.science/hal-03489546v1>**

Submitted on 7 Mar 2022

**HAL** is a multi-disciplinary open access archive for the deposit and dissemination of scientific research documents, whether they are published or not. The documents may come from teaching and research institutions in France or abroad, or from public or private research centers.

L'archive ouverte pluridisciplinaire **HAL**, est destinée au dépôt et à la diffusion de documents scientifiques de niveau recherche, publiés ou non, émanant des établissements d'enseignement et de recherche français ou étrangers, des laboratoires publics ou privés.



Distributed under a Creative Commons Attribution - NonCommercial 4.0 International License

# 1 **Rain gauge networks' limitations and the implications** 2 **to hydrological modelling highlighted with a X-band** 3 **radar**

4

5 Igor Paz<sup>1,2</sup>, Ioulia Tchiguirinskaia<sup>1</sup> and Daniel Schertzer<sup>1</sup>

6

7 <sup>1</sup> HMCO, École des Ponts ParisTech, University of Paris-Est, Champs-sur-Marne 77455,  
8 France; ioulia.tchiguirinskaia@enpc.fr (I.T.); daniel.schertzer@enpc.fr (D.S.)

9 <sup>2</sup> Instituto Militar de Engenharia, Praça General Tibúrcio 80, Rio de Janeiro 22290-270, Brazil

10 \* Correspondence: igor.da-silva-rocha-paz@enpc.fr

11

## 12 **Abstract**

13       Precipitation risk and water management is a key challenge for densely  
14 populated urban areas. Applications derived from high spatio-temporal  
15 resolution observation of precipitations are to make our cities more weather-  
16 ready. Finer resolution data available from dual polarised X-band radar  
17 measurements enhance engineering tools as used for urban planning policies  
18 as well as protection (mitigation/adaptation) strategies to tackle climate-change  
19 related weather events. For decades engineering tools have been developed to  
20 work conveniently either with very local rain gauge networks, or with mainly C-  
21 band radars that have gradually been set up for space-time remote sensing of  
22 precipitation. Most of the time, the C-band radars continue to be calibrated by  
23 the existing rain gauge networks. Inhomogeneous distributions of these  
24 networks lead to only a partial information on the rainfall fields. Here we show  
25 that the statistics of measured rainfall is strongly biased by the fractality of the

26 measuring networks and that this fractality needs to be properly taken into  
27 account to retrieve the original properties of the rainfall fields, in spite of the  
28 radar data calibration. In this work, we use the semi-distributed hydrological  
29 modelling over the Bièvre catchment to generate a virtual rain gauges' network.  
30 And, firstly, performing a fractal analysis of this network distribution, we  
31 demonstrate that the semi-distributed hydrological models statistically reduce  
32 the distributed (weather radar) rainfall fields into rainfall measured by a much  
33 scarcer network of virtual rain gauges. Then, with the help of the Intersection  
34 Theorem and multifractal theory, we statistically compare the virtual rain  
35 gauges' data with the rainfall data measured by the dual-polarimetric X-band  
36 radar operated at Ecole des Ponts with a spatial resolution of 250 m, providing  
37 pre-factors that indicate the need of a proper re-normalisation of rain gauge  
38 rainfall data when comparing (or calibrating) with radar data and the possible  
39 counterproductivity of this conditioning.

40

41 **Keywords:** rain gauge network; spatio-temporal variability; X-band radar;  
42 fractals; multifractals; semi-distributed hydrological model

43

## 44 **1. Introduction**

45 The increase in global urbanisation and population density emphasises  
46 the importance and the need to improve the adaptation of urban areas mainly to  
47 climate change (Pumo et al., 2017; Arnone et al., 2018). Managing extreme  
48 weather events, particularly intense precipitation ones and heat waves, in these  
49 areas is a major challenge for the future. The population's demand for a better  
50 quality of life motivates an improvement in the ability to measure, understand,

51 model and predict hydrometeorological processes in urban environments,  
52 aiming at better flood control and associated risk management. Conventional  
53 local measurements in urban areas generally do not meet the World  
54 Meteorological Organization (WMO) criteria for the measurement of  
55 precipitation (WMO, 2014). Better spatio-temporal scales with accuracy and  
56 reliability are required (Fabry et al., 1994; Berne et al., 2004). In this way, the  
57 use of ground-based remote sensing has been very important in elucidating  
58 complex urban environment structures, thus expanding hydrometeorological  
59 challenges (NRC, 2012).

60         Weather radars have the capability to estimate rainfall fields with high  
61 spatio-temporal resolutions and have been used to cope the sparseness of rain  
62 gauge networks. Nevertheless, the initial measurement of reflectivities adopted  
63 by those devices, not providing direct precipitation rates such as rain gauges,  
64 usually generates significant uncertainties. Then, with the growing use of radars  
65 to estimate rain rates, many studies have been developed to adjust and/or  
66 merge weather radars (mostly considering non-polarimetric ones) with rain  
67 gauge networks (Einfalt et al., 2005; Allegretti et al., 2012; Lo Conti et al.,  
68 2015). On the other hand, especially for high rainfall intensities, in order to  
69 reduce these uncertainties and improve the rainfall estimates, dual polarisation  
70 technology using specific differential phase (KDP) has been employed, which  
71 does not necessarily requires rain gauge adjustments according to some  
72 authors (Bringi and Chandrasekar 2001; Illingworth and Blackman 2002;  
73 Figueras i Ventura et al., 2012; Chandressekar et al., 2015). This technology  
74 explores the flatness of large raindrops to analyse the phase difference of the

75 reflected vertical and horizontal signals and then directly obtain the precipitation  
76 rates.

77 Coming together with rainfall data improvement, an efficient storm water  
78 management also deals with the accuracy and reliability of hydrological models,  
79 mainly in urban areas which present higher levels of imperviousness leading to  
80 shorter response times (Berne et al., 2004; Segond et al., 2007; Furusho et al.,  
81 2014; Ochoa-Rodriguez et al., 2015; Arnone et al., 2018). This requests the use  
82 of high resolution models, which means reducing the size of the sub-  
83 catchments in the semi-distributed models or adopting the fully-distributed  
84 models (Fewtrell et al., 2011; Ichiba, 2016; Pina et al., 2016; Pumo et al., 2017;  
85 Alves de Souza et al., 2018; Paz et al., 2019).

86 This work presents a discussion of the rain gauge networks' limitations  
87 and the implications to hydrological modelling with the help of fractal and  
88 multifractal analysis. The study was carried out over the Bièvre catchment,  
89 which is a 110 km<sup>2</sup> semi-urbanised area located in the southwest of Paris  
90 region, using the rainfall data of the dual-polarimetric X-band radar recently  
91 installed on the roof of the École des Ponts ParisTech (ENPC).

92 The paper is organised in five sections. Section 2 describes the case  
93 study and the rainfall data. The methodology of fractal and multifractal analyses  
94 are presented in Section 3. Section 4 presents the results and discussion. And  
95 finally, the conclusions are presented in Section 5.

96

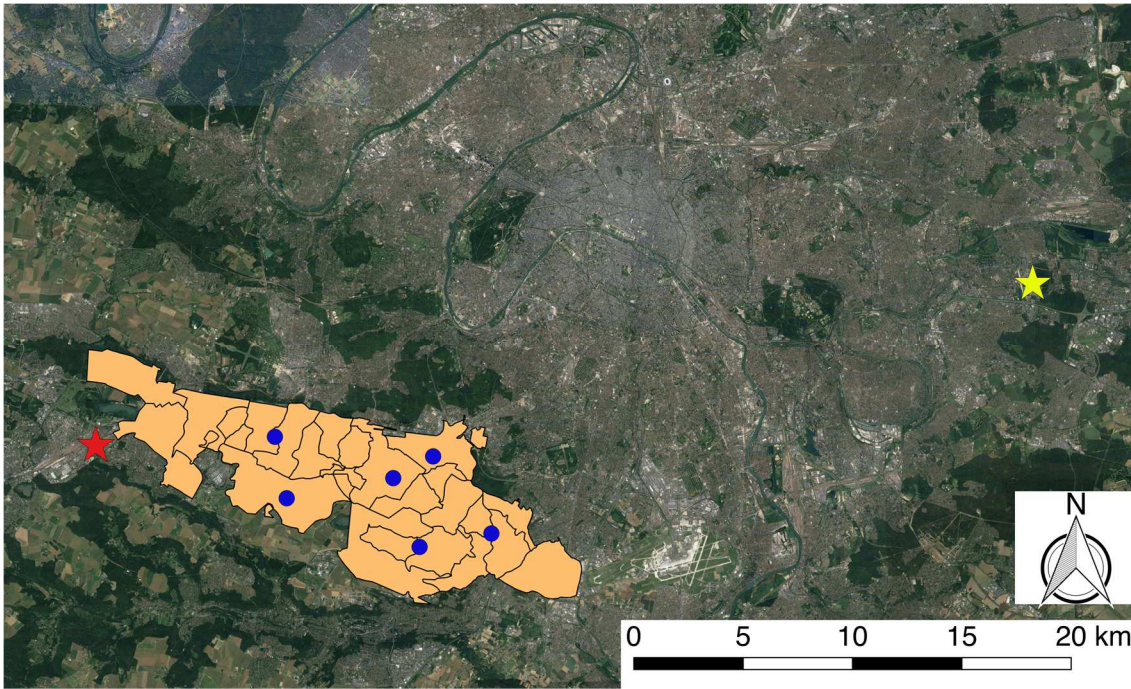
## 97 **2. Case Study and Rainfall Data**

98 The Bièvre Valley, which is a 110 km<sup>2</sup> semi-urbanised area in the  
99 southwest of Paris region, was selected as case study. The Bièvre River is 33

100 km-long tributary of the Seine River and its upstream catchment is managed by  
101 two local authorities: the CASQY (“Communauté d’Agglomération de Saint-  
102 Quentin-en-Yvelines” – Saint-Quentin-en-Yvelines Agglomération Community)  
103 in the upstream portion and the SIAVB (“Syndicat Intercommunal  
104 d’Assainissement de la Vallée de la Bièvre” – Inter-municipal local authority for  
105 Sanitation of the Bièvre Valley) in the downstream portion.

106         The Bièvre catchment was modelled using InfoWorks CS (Collection  
107 Systems) (Paz, 2018; Paz et al., 2018), a widely used semi-distributed model  
108 (Soft, 2010), with the operation responsibility given to the company Veolia since  
109 1991 by the local authority SIAVB to perform a real time control of the  
110 hydrological area. This hydrological model is integrated in the Optim Sim  
111 platform, developed by Veolia, that mimics the actual regulation of the storage  
112 basins (Paz, 2018; Paz et al., 2018) in two simulation modes: the “replay mode”  
113 and the “forecasting mode”. The first one extracts rainfall data from the 6 SIAVB  
114 rain gauges’ network database (using the Thiessen polygons technique) to  
115 replay past events. And the “forecasting mode” uses different rainfall data, e.g.  
116 from weather radar measurements, to simulate the catchment hydrological  
117 behaviour. The catchment area is divided into 27 sub-catchments, as displayed  
118 on Figure 1.

119



120

121 *Figure 1: Illustration of rainfall measurement devices available over the Bièvre catchment: the X-band radar (yellow*  
 122 *star), the C-band radar (red star) and the six rain gauges (blue dots).*

123 This modelling had been firstly calibrated using the rainfall data from the  
 124 Météo-France C-band radar of Trappes, located in a direct proximity (~ 0 - 20  
 125 km) of the catchment (see Fig. 1), with a resolution of 1 km x 1 km x 5 min.  
 126 These C-band radar data are firstly obtained as reflectivity (dBZ) and then, after  
 127 some post-treatments and filtering process, they are transformed into rainfall  
 128 intensity (R) by applying the Marshall-Palmer Z-R equation (Marshall and  
 129 Palmer, 1948), with fixed parameters  $a = 200$  and  $b = 1.6$  (Eq. (1)), which  
 130 means that the polarimetric capability of this radar of Trappes has not been  
 131 used. In addition, this catchment also contains a network of six tipping bucket  
 132 rain gauges (see Fig. 1), which had been used to calibrate the C-band radar  
 133 data.

$$Z = aR^b \quad (1)$$

134

135           However, in this study, we used rainfall data from the ENPC dual-  
136 polarimetric X-band radar of Champs-sur-Marne (see Fig. 1), with distances  
137 ranging between 25 to 45 km and a 250 m x 250 m x 3.41 min resolution. The  
138 ENPC X-band Dual Polarization Surface Rainfall Intensity (DPSRI) product still  
139 considers the Z-R relationship for low intensities, but for high intensities it uses  
140 the specific differential phase (KDP) (Selex, 2015):

$$R = 19.63|KDP|^{0.823}, \text{ for } Z > 35 \text{ dBZ and } KDP > 0.3^\circ/\text{km} \quad (2)$$

141

142           For the purpose of this work, six different rainfall events were selected:  
143 12-13/09/2015 (44 hours); 16/09/2015 (11.3 hours); 05-06/10/2015 (31 hours);  
144 21-23/05/2016 (59.5 hours); 28-31/05/2016 (87.7 hours); and 17/06/2016 (24  
145 hours).

146

### 147 **3. Methods: (multi)fractals**

148           When studying some objects of very irregular or fragmented form (with  
149 unusual properties in classical geometry), Mandelbrot (1974) named them as  
150 “fractals” (“fractus” means irregular in Latin). Nevertheless, fractal objects must  
151 not just be irregular, but also scale invariant, which means that their form  
152 remains unchanged at different scales of observation. This brings the properties  
153 of self-similarity (a zoomed part of the object looks similar to the object itself,  
154 with an isotropic variation) and self-affinity (when the variation is anisotropic).

155           In classical geometry, dimensions are integers characterising regular  
156 spaces as straight lines (1D), planar figures (2D) and volumes (3D). If we take  
157 an object, embedded in an Euclidian dimension  $D$ , of linear size  $L$ , it can be  
158 covered by  $N$  small objects of linear size  $l$ , with a scale ratio  $\lambda (= L/l)$ .



159 In the case of fractal objects and sets, the dimension is no longer an  
160 integer and is called fractal dimension ( $D_f$ ) (Mandelbrot, 1967, 1977;  
161 Mandelbrot and Pignoni, 1983; Feder, 1988). Even if its theoretical computation  
162 is rather complex, an easier way to evaluate it is through the box-counting  
163 method (Hentschel and Procaccia, 1983; Lovejoy et al., 1987). It takes into  
164 account that when  $\lambda \rightarrow \infty$  there is a power-law relation between the fractal  
165 dimension and the number of “non-empty” pixels of the set ( $N_\lambda$ ) at the scale  $\lambda$ :

$$N_\lambda \approx \lambda^{D_f} \quad (3)$$

166

167 where  $\approx$  means the asymptotic equivalence.

168 Therefore, the box-counting method can be easily applied considering a  
169 simple methodology to change the resolution of a given dataset. Let us define  $A$   
170 as the geometrical set (embedded in a space of dimension  $D$ ; in this paper we  
171 will consider the 2-D space) to be analysed and  $N_{\lambda,A}$  the number of non-  
172 overlapping pixels at the resolution  $\lambda$  necessary to cover the set  $A$ . Thus, the  
173 method consists in firstly counting the number of non-empty pixels at the  
174 smallest pixel size ( $l$ ), then we multiply the pixel size by two at each step of  
175 process (practically, it means that in the 2-D case we merge 4 by 4 pixels at  
176 each scale variation step) and count again the number of non-empty pixels at  
177 this new size, and we continue this procedure until we achieve the maximum  
178 pixel size ( $L$ ). Once we have counted the numbers of non-empty pixels ( $N_\lambda$ ) at  
179 different scales ( $\lambda$ ), we display them in a log-log plot ( $\lambda$  vs  $N_\lambda$ ). Then, if  $A$  is a  
180 fractal set, the points of this plot will be along a straight line, and, from Eq. (1),  
181 we can estimate the fractal dimension  $D_f$  as its slope.

182 Furthermore, the codimension of a fractal set is usually (geometrically)  
183 defined as (Mandelbrot, 1967, 1977; Feder, 1988; Falconer, 1990):

$$c = D - D_f \tag{4}$$

184

185 Then, it is also possible to probabilistically define the fractal codimension,  
186 using Eqs. (3) and (4), where the probability that a cube embedded in the set  
187  $\mathbb{R}^D$  at a scale  $\lambda$  is contained in the fractal set is given by:

$$\lambda^{D-D_f} \approx \lambda^c \tag{5}$$

188 This last definition is more general because it enables  $c > D$ , which  
189 would imply  $D_f < 0$  from Eq. (4).

190 The concept of fractal dimension is related to the sparseness of a  
191 dataset and it is well applied to binary fields (e.g., rainfall occurrence, rain  
192 gauge network distribution). Many geophysical fields with different intensity  
193 levels, and also irregular geometries and scale invariance, can be seen as  
194 fractal fields at different thresholds (singularities). Then, for each singularity it is  
195 possible to calculate its fractal dimension, which means that the field is  
196 characterised by several fractal dimensions according to the imposed threshold  
197 (Grassberger, 1983; Hentschel and Procaccia, 1983; Schertzer and Lovejoy,  
198 1984); i.e., for each given threshold, a different fractal dimension is estimated  
199 for the field that exceeds the threshold. These fields were named by Parisi and  
200 Frisch (1985) as “multifractals”.

201 Multifractals rely on the assumption that a geophysical field is generated  
202 through a multiplicative cascade process (Schertzer and Lovejoy, 1987, 2011)

203 produced by random multiplicative modulation of large-scale structures into  
 204 small-scale ones. Furthermore, rainfall fields have been widely studied as  
 205 presenting multifractal behaviour (Schertzer and Lovejoy, 1987; Ladoy et al.,  
 206 1993; Tessier et al., 1993; Olsson et al., 1996; de Lima et al., 1999; Deidda,  
 207 2000; Veneziano et al., 2006; García-Marin et al., 2008; Serinaldi, 2010;  
 208 Ochoa-Rodriguez et al., 2015; Paz, 2018).

209 As just mentioned, the multifractal fields are characterised by a hierarchy  
 210 of fractal dimensions (and codimensions). Then, by referring to the notion of  
 211 fractal codimension, one can calculate, for a given multifractal field  $\varepsilon_\lambda$ , the  
 212 probability of obtaining a singularity of order greater than or equal to  $\gamma$  at the  
 213 scale  $\lambda$ :

$$\Pr(\varepsilon_\lambda \geq \lambda^\gamma) = \frac{\lambda^{D_f(\gamma)}}{\lambda^D} \approx \lambda^{-c(\gamma)} \quad 6)$$

214

215 where the codimension function  $c(\gamma) = D - D_f(\gamma)$  is convex and increases with  
 216  $\lambda$ .

217 Additionally, multifractal fields can also be described by their statistical  
 218 moments. Schertzer and Lovejoy (1987, 1991) introduced the scaling moment  
 219 function  $K(q)$ , which is also convex and characterises the various  $q^{th}$  order  
 220 statistical moments of the multifractal field  $\varepsilon_\lambda$ :

$$\langle \varepsilon_\lambda^q \rangle \approx \lambda^{K(q)} \quad 7)$$

221

222 where  $q$  is the statistical moments order and  $\langle \varepsilon_\lambda^q \rangle$  is the  $q^{th}$  moment mean of the  
 223 intensities at the scale  $\lambda$ .

224 Furthermore, Parisi and Frisch (1985) demonstrated that the two  
 225 functions  $c(\gamma)$  and  $K(q)$  have a one-to-one relationship, which is highlighted by  
 226 the Legendre transform:

$$K(q) = \max_{\gamma}\{q\gamma - c(\gamma)\} \Leftrightarrow c(\gamma) = \max_q\{q\gamma - K(q)\}$$

8)

227

228 These related expressions bring the correspondence between the orders  
 229 of moments ( $q$ ) and the singularities ( $\gamma$ ), such that:

$$q_{\gamma} = c'(\gamma) ; c(\gamma) = q_{\gamma}\gamma - K(q_{\gamma}) \quad (9)$$

$$\gamma_q = K'(q) ; K(q) = q\gamma_q - c(\gamma_q) \quad (10)$$

230

231 where at the moment of order  $q$  corresponds the singularity  $\gamma_q$ , and conversely,  
 232 at the singularity  $\gamma$  corresponds the order of moment  $q_{\gamma}$ . In addition, it is  
 233 possible to see from Eq. (6) that more rare rainfall events (with very large  
 234 singularities  $\gamma$ ) correspond to bigger values of  $c(\gamma)$ . Consequently, due to the  
 235 convexity of both  $c(\gamma)$  and  $K(q)$  and to the Legendre transform, for  $q > 1$ , these  
 236 extreme events also correspond to bigger values of  $q$  and  $K(q)$ .

237 As both statistical functions  $c(\gamma)$  and  $K(q)$  have the only constraint of  
 238 convexity, there is an infinity of parameters required to characterise a  
 239 multifractal process. However, Schertzer and Lovejoy (1987, 1997) explored the  
 240 concept of universality (usually used in physics, where among an infinite  
 241 number of parameters only a few would be relevant) and developed the  
 242 Universal Multifractals (UM) (see Schertzer and Lovejoy, 2011, for a more  
 243 recent review). In this context,  $c(\gamma)$  and  $K(q)$  can be fully described by only  
 244 three "UM parameters" ( $\alpha$ ,  $C_1$  and  $H$ ) as:

$$K(q) = q^H + \begin{cases} \frac{C_1}{\alpha - 1} (q^\alpha - q); & \alpha \neq 1 \\ C_1 q \log(q) & ; \alpha = 1 \end{cases} \quad (1)$$

$$c(\gamma + H) = \begin{cases} C_1 \left( \frac{\gamma}{C_1 \alpha'} + \frac{1}{\alpha} \right)^{\alpha'} & ; \alpha \neq 1 \\ C_1 \exp\left(\frac{\gamma}{C_1} - 1\right) & ; \alpha = 1 \end{cases} \quad (2)$$

245

246 where  $\frac{1}{\alpha} + \frac{1}{\alpha'} = 1$ , for all  $\alpha \neq 1$ , and:

247 –  $\alpha$  is the Levy's multifractality index ( $0 \leq \alpha \leq 2$ ). It measures the degree of  
 248 multifractality of the process. In particular, if  $\alpha = 0$  we observe a monofractal  
 249 process (also entitled  $\beta$ -model, Mandelbrot (1974)) and  $\alpha = 2$  corresponds to  
 250 the maximum of multifractality for a model (improperly called lognormal);

251 –  $C_1$  is the codimension of the mean singularity of the field. It measures the  
 252 mean inhomogeneity, where  $C_1 = 0$  for a homogeneous field. The more it  
 253 increases, the more the singularity of the field average is dispersed. We thus  
 254 observe a field rarely exceeding its mean, but which can do so in an  
 255 extremely strong way;

256 –  $H$  is the Hurst's exponent, which measures the degree of non-conservation of  
 257 the field. Values of  $H$  close to zero indicate higher conservativeness of the  
 258 process.

259

260 While performing a multifractal analysis of a (rainfall) field, we should  
 261 determine its statistical functions  $c(\gamma)$  and  $K(q)$ . The Trace Moment (TM)  
 262 method (Schertzer and Lovejoy, 1987) allows to directly determine the scaling  
 263 moments function  $K(q)$  for any  $q > 0$ .

264 As  $K(q) > 0$  for  $q > 1$ ,  $\langle \varepsilon_\lambda^q \rangle \approx \lambda^{K(q)} \rightarrow \infty$  when  $\lambda \rightarrow \infty$ . Then, to avoid this  
 265 divergence, the concept of flux ( $\Pi_\lambda$ ) is used, given by:

$$\Pi_\lambda = \int \varepsilon_\lambda d^D x \quad (13)$$

266

267 And the trace of the  $q^{th}$ -power of the flux is:

$$Tr[\varepsilon_\lambda^q] = \left\langle \int (\varepsilon_\lambda)^q d^{qD} x \right\rangle \approx \lambda^{K(q)-D(q-1)} \quad (14)$$

268

269 In practice, the method consists in taking the  $q^{th}$ -power of each value of  
 270 the field  $\varepsilon_\lambda$  at the scale  $\lambda$ , and then the ensemble average of  $q^{th}$ -power  
 271 moments is calculated at that scale. Then, from Eq. (14), the same process is  
 272 repeated for different scales  $\lambda$ , the resulting averages are displayed as a  
 273 function of  $\lambda$  in a log-log plot, and a linear regression is performed to obtain the  
 274 value of  $K(q)$  (which will be estimated as the given slope). Finally, by repeating  
 275 this process also with other values of  $q$ , we obtain the  $K(q)$  function (and, via  
 276 Legendre transform, the  $c(\gamma)$  function).

277 Thus, once we know  $K(q)$ , it is possible to (indirectly) determine the UM  
 278 parameters  $\alpha$  and  $C_1$ :

$$C_1 = K'(1) \quad (15)$$

$$\alpha = K''(1)/C_1 \quad (16)$$

279

280 In the framework of UM, Lavallée et al. (1993) developed the Double  
 281 Trace Moment (DTM) method to directly determine the parameters  $\alpha$  and  $C_1$ ,  
 282 which means that there is no need to firstly obtain  $K(q)$  (and  $c(\gamma)$ ). This

283 technique is in fact a generalisation of the TM method and considers that the  
 284  $q^{th}$ -order moments of the renormalised  $\eta$ -power of a conservative field  $\varepsilon_\lambda$   
 285 remain scale invariant. Then, the idea is to apply the TM method to this  
 286 renormalised field (through the  $K(q, \eta)$  function):

$$\langle (\varepsilon_\lambda^{(\eta)})^q \rangle \approx \lambda^{K(q, \eta)} \Rightarrow \frac{\langle \varepsilon_\lambda^{\eta q} \rangle}{\langle \varepsilon_\lambda^\eta \rangle^q} \approx \frac{\lambda^{K(q\eta)}}{\lambda^{qK(\eta)}} = \lambda^{K(q\eta) - qK(\eta)} \quad (1)$$

7)

287 where  $\varepsilon_\lambda^{(\eta)} = \frac{\varepsilon_\lambda^\eta}{\langle \varepsilon_\lambda^\eta \rangle}$ .

288 Then:

$$K(q, \eta) = K(q\eta) - qK(\eta) \quad (1)$$

8)

289

290 Since this method is especially applied for UM, considering Eq. (11), Eq.  
 291 (18) becomes:

$$K(q, \eta) = \eta^\alpha K(q) \quad (1)$$

9)

292 From Eq. (19), the parameter  $\alpha$  can be directly estimated as the slope of  
 293 the linear part of  $K(q, \eta)$  vs.  $\eta$  in a log-log plot, for a given  $q$ . And in the same  
 294 log-log plot, the parameter  $C_1$  can be also estimated from the interception value  
 295 of the linear part and the axis  $\log(\eta) = 0$  (Hoang, 2011).

296 In addition, according to the Intersection Theorem (Schertzer and  
 297 Lovejoy, 1987), considering two independent (multi)fractal fields  $\varepsilon_{1,\lambda}$  and  $\varepsilon_{2,\lambda}$   
 298 embedded in the same space and presuming that the intersection of both ( $\varepsilon_{1,\lambda} \cap$   
 299  $\varepsilon_{2,\lambda}$ ) is not empty, for the given intersection the probability of obtaining a  
 300 singularity of order greater than or equal to  $\gamma$  at the scale  $\lambda$  is:

$$\Pr(\varepsilon_{1,\lambda} \cap \varepsilon_{2,\lambda} \geq \lambda^\gamma) = \Pr(\varepsilon_{1,\lambda} \geq \lambda^\gamma) \Pr(\varepsilon_{2,\lambda} \geq \lambda^\gamma)$$

20)

301

302 Therefore, following Eq. (6), the resulting codimension is the addition of  
 303 independent (multi)fractal processes:

$$c_{\varepsilon_1 \cap \varepsilon_2}(\gamma) = c_{\varepsilon_1}(\gamma) + c_{\varepsilon_2}(\gamma)$$

21)

304

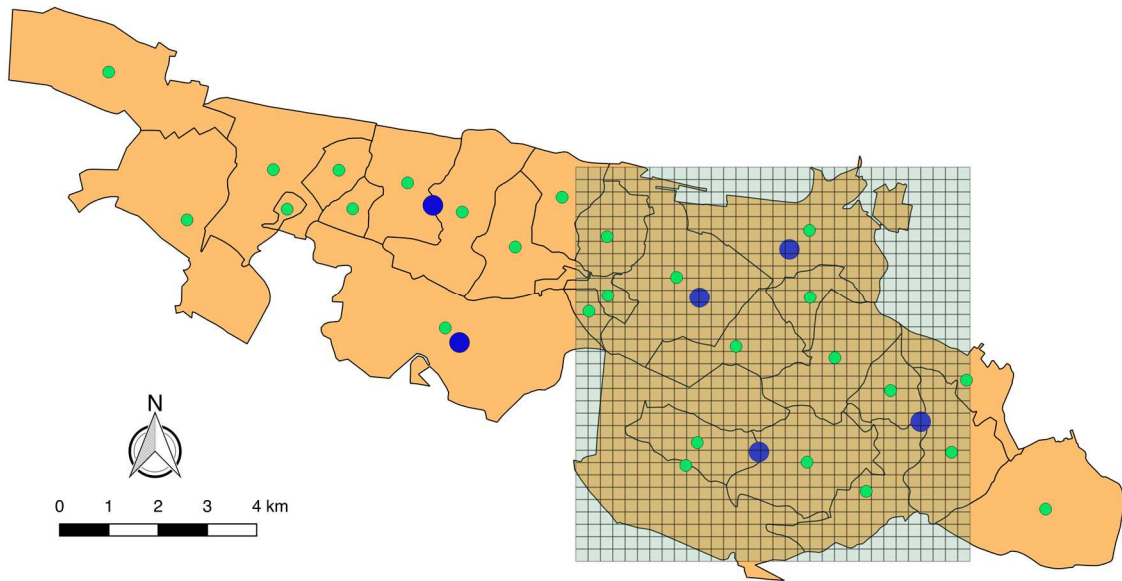
305 In the following Section, we will use the fractal and multifractal (with the  
 306 help of the DTM method and the Intersection Theorem) approaches to discuss  
 307 the rain gauge networks' limitations and the implications to hydrological  
 308 modelling.

309

#### 310 **4. Results and Discussion**

311 In this work, the sub-catchments' distribution of the pilot site of Bièvre  
 312 catchment, which had already been modelled with the semi-distributed model  
 313 InfoWorks CS (Paz, 2018; Paz et al., 2018), was used to construct a network of  
 314 virtual rain gauges located in the centre of mass of each sub-catchment. Then,  
 315 an area of 8 km x 8 km was selected using the X-band radar grid (Fig. 2). This  
 316 choice corresponds to the most homogeneous distribution of virtual rain gauges  
 317 over a square area of Bièvre catchment, containing 15 of the 27 virtual rain  
 318 gauges.



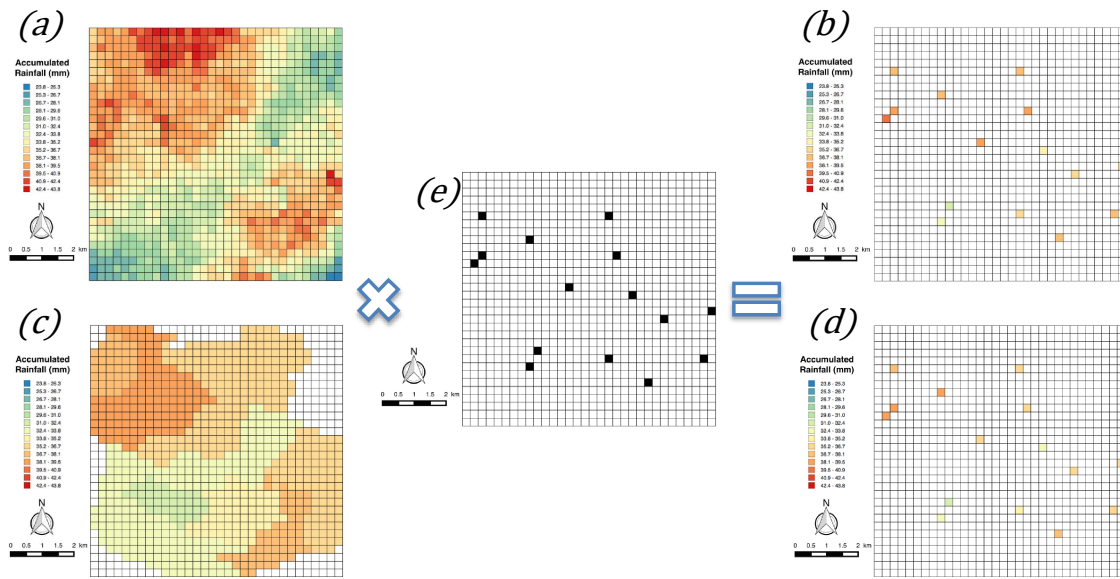


319

320 Figure 2: Virtual rain gauges' distribution (green dots) and 6 SIAVB rain gauges  
 321 (blue dots) over the 27 sub-catchments, and the 8 km x 8 km selected ENPC X-band  
 322 radar grid.

323

324 Four different rainfall fields have been analysed over the selected area  
 325 (Fig. 3): (a) original radar data; (b) original radar data corresponding to each  
 326 centroid pixel; (c) sub-catchment averaged rainfall radar data; (d) sub-  
 327 catchment averaged rainfall radar data being concentrated at the corresponding  
 328 centroid pixel; as well as a (e) fractal distribution of the corresponding virtual  
 329 rain gauges, located at the centroid pixels.



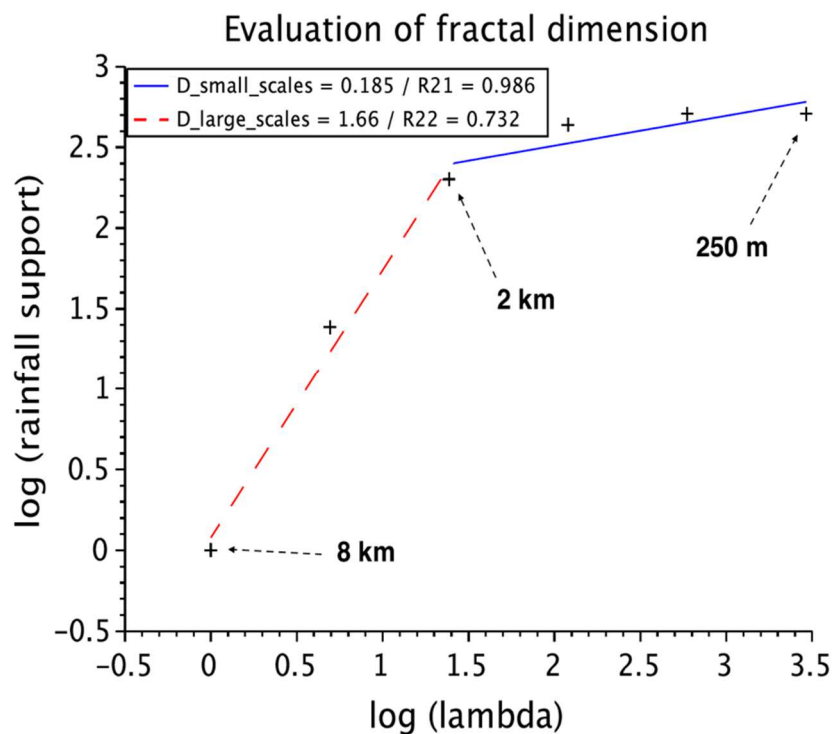
330  
331

332 Figure 3: Four different rainfall radar data fields analysed over the  
 333 selected area (demonstrated here with data of the 12 September 2015 event):  
 334 (a) original data; (b) original data corresponding to each centroid pixel; (c) sub-  
 335 catchment averaged rainfall; (d) sub-catchment averaged rainfall being  
 336 concentrated at the corresponding centroid pixels. And the 15 sub-catchment  
 337 centroid pixels corresponding to the virtual rain gauges' locations (e).

338

339 Firstly, the fractal analysis of the 15 virtual rain gauge pixels' distribution  
 340 (which will also be called rainfall support) was performed using the box-counting  
 341 method (Fig. 4) with a simple Scilab routine (Gires et al., 2017, 2018), which  
 342 applies the methodology described in the previous section (see Eq. (3)) to the  
 343 dataset. It is possible to identify a scaling break (with two different behaviours  
 344 for the small scales and the large scales) at the spatial scale of 2 km, which is in  
 345 fact the average sub-catchment's size and close to the 1-km resolution of the C-  
 346 band radar rainfall data that have been used for the model calibration. Then, a  
 347 relatively high fractal dimension ( $D_f = 1.66$ ) obtained over the large-scale range

348 corresponds to the network of 15 virtual rain gauges at 2-km scale. This number  
 349 of gauges remains still reasonable, although only 6 real rain gauges are  
 350 available for the full Bièvre catchment (i.e. 4 over the selected area). Preserving  
 351 the same fractal dimension  $D_f = 1.66$  over smaller scales up to 250 m (the  
 352 resolution of the X-band radar rainfall) would result in  $N = 315$  virtual rain  
 353 gauges (and/or sub-catchments). Thus, a smaller number of gauges ( $N = 15$ ),  
 354 characterised by much lower fractal dimension ( $D_f = 0.185$ ), significantly  
 355 reduces the captivity of spatial rainfall variability over small scales and hence its  
 356 representability in the model having a constant rainfall per sub-catchment of 2-  
 357 km characteristic scale.



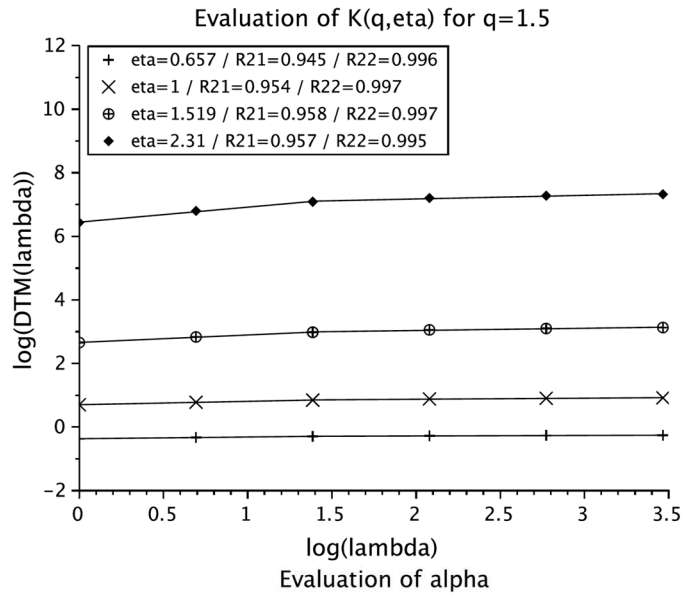
358

359 *Figure 4: Fractal analysis of the centroid pixels' distribution, providing the linear regression coefficients R21 (small*  
 360 *scales) and R22 (large scales).*

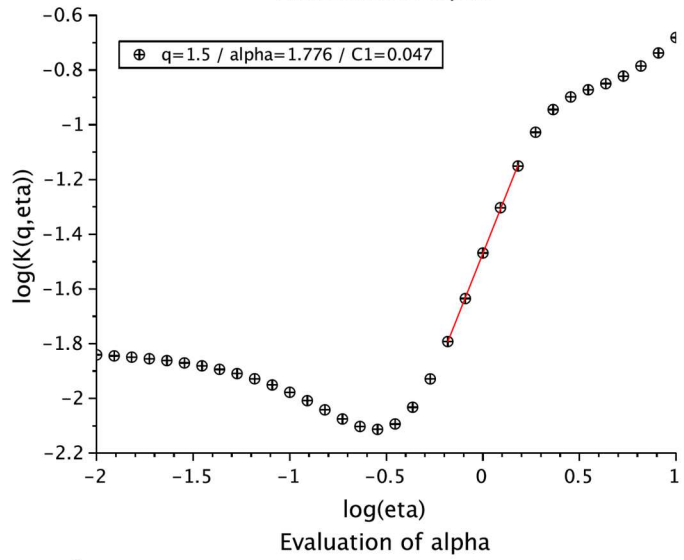
361 This result from the fractal analysis of the 15 virtual rain gauge network  
 362 distribution corroborates the researches from Austin (1987), Schertzer and  
 363 Lovejoy (1987), Seed and Austin (1990), Vieux and Vieux (2005), Villarini et al.

364 (2008), Peleg et al. (2013), which identify the difficulties of sparsely distributed  
365 rain gauge networks to capture the high spatial and temporal variability of  
366 precipitation fields (specially high convective ones), while comparing to weather  
367 radars. On the other hand, when dealing with the sub-catchment sizes, it also  
368 confirms the findings of Thorndahl et al. (2017), based on a review of the state  
369 of the art about the use of weather radar rainfall data in urban hydrology  
370 (Schilling, 1991; Berne et al., 2004; Einfalt et al., 2004; Ochoa-Rodriguez et al.,  
371 2015), in which they associate the better spatial and temporal resolution of  
372 radar rainfall data to decreasing catchment sizes.

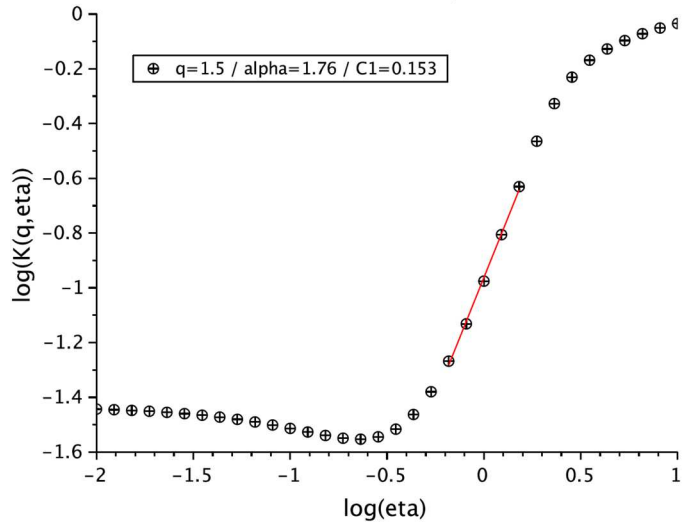
373         Then, to better evaluate the unfortunate consequences of sparse rain  
374 gauge networks, the multifractal analyses were performed over the studied  
375 rainfall fields in conditions (a), (b), (c) and (d), and then related to the fractal  
376 analysis of the rain gauge's distribution with the help of the Legendre transform.  
377 Firstly, the DTM method was applied (Fig. 5), following the methodology  
378 described in Section 3 (Eq. (19)), on ensemble of data over the whole rainfall  
379 event (each time step being considered as an independent realisation) with  
380 scaling break. The values obtained for  $\alpha$  and  $C_1$  for the six studied events are  
381 presented at Tables: 1 (rainfall fields (a)), 2 (rainfall fields (b)), 3 (rainfall fields  
382 (c)) and 4 (rainfall fields (d)).



383



384



385

386

Figure 5: Application of DTM method (demonstrated here with data of the 12-

387

13 September 2015 event): Evaluation of empirical  $K(q, \eta)$  with scaling break at 2 km,

388 providing the linear regression coefficients R21 (small scales) and R22 (large scales)  
 389 (top); Evaluation of  $\alpha$  at small scales (centre); Evaluation of  $\alpha$  at large scales (bottom).

390

391

Events	Small Scales		Large Scales	
	$\alpha$	$C_1$	$\alpha$	$C_1$
12-13/09/2015	1.776	0.047	1.76	0.153
16/09/2015	1.676	0.027	0.922	0.094
05-06/10/2015	2.029	0.05	1.775	0.189
21-23/05/2016	1.324	0.041	1.242	0.161
28-31/05/2016	1.656	0.045	1.665	0.199
17/06/2016	1.305	0.127	1.058	0.574

392

*Table 1: Estimated UM parameters for rainfall fields in condition (a).*

393

Events	Small Scales		Large Scales	
	$\alpha$	$C_1$	$\alpha$	$C_1$
12-13/09/2015	-0.009	1.757	0.746	0.659
16/09/2015	0.023	1.769	0.244	0.539
05-06/10/2015	0.07	1.788	0.636	0.623
21-23/05/2016	0.015	1.778	0.295	0.571
28-31/05/2016	-0.003	1.761	0.613	0.64
17/06/2016	-0.009	1.753	0.487	1.016

394

*Table 2: Estimated UM parameters for rainfall fields in condition (b).*

395

Events	Small Scales		Large Scales	
	$\alpha$	$C_1$	$\alpha$	$C_1$
12-13/09/2015	0.642	0.087	1.397	0.131

16/09/2015	0.247	0.075	0.602	0.092
05-06/10/2015	0.684	0.09	1.421	0.152
21-23/05/2016	0.309	0.083	0.844	0.127
28-31/05/2016	0.493	0.084	1.31	0.149
17/06/2016	0.661	0.123	0.969	0.341

396

*Table 3: Estimated UM parameters for rainfall fields in condition (c).*

397

Events	Small Scales		Large Scales	
	$\alpha$	$C_1$	$\alpha$	$C_1$
12-13/09/2015	-0.014	1.751	0.66	0.6
16/09/2015	0.011	1.762	0.153	0.514
05-06/10/2015	0.039	1.769	0.515	0.591
21-23/05/2016	-0.003	1.763	0.278	0.545
28-31/05/2016	-0.019	1.75	0.587	0.601
17/06/2016	-0.006	1.749	0.545	0.871

398

*Table 4: Estimated UM parameters for rainfall fields in condition (d).*

399

400 Due to the fact that the rainfall fields (condition (a)) and the virtual rain  
401 gauge's network distribution (condition (e)) are fully independent, the  
402 Intersection theorem (see Section 3) implies that the codimension function of  
403 their product (condition (b)) will correspond to the following sum of the  
404 codimension functions:

$$c_{(b)=(a)\cap(e)}(\gamma) = c_{(a)}(\gamma) + c_{(e)}(\gamma)$$

22)

405

406 And then, by Legendre transform (see Section 3), the scaling moment  
407 function of the product (condition (b)) will correspond to the sum of the scaling

408 moment functions of the rainfall field (condition (a)) and the virtual rain gauge  
409 network (condition (e)):

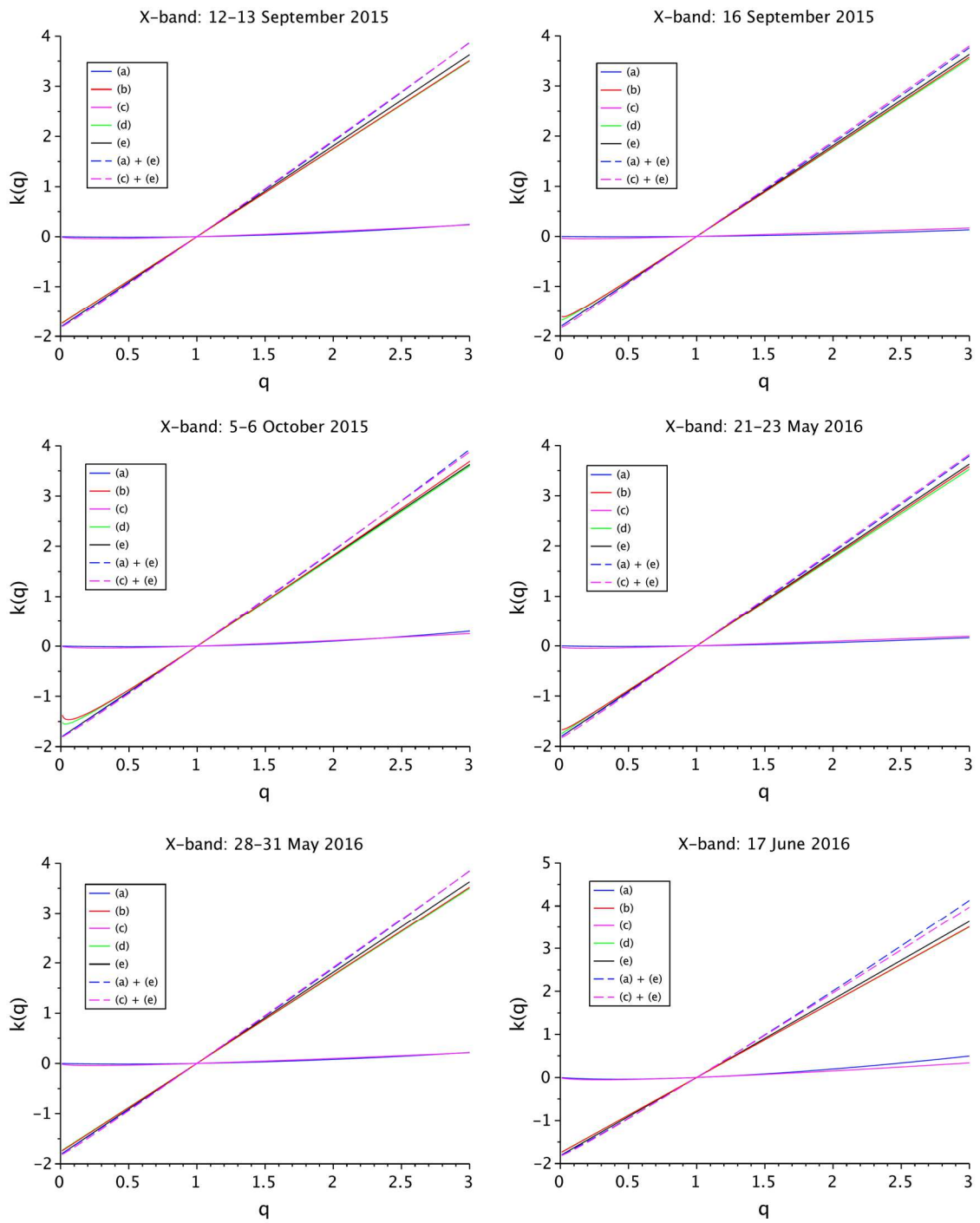
$$K_{(b)=(a)\cap(e)}(q) = K_{(a)}(q) + K_{(e)}(q) \quad 23)$$

410

411 The relationships similar to Eqs. (22) and (23) stand for the rainfall fields  
412 (condition (c)), virtual rain gauge network (condition (e)) and their product  
413 (condition (d)) as well. Figures 6 and 7 present the theoretical  $K(q)$  curves for  
414 all fields taking into account the estimated values (from Fig. 4 and Tables 1, 2, 3  
415 and 4), for small scales (250 m – 2 km) and large scales (2 km - 8 km)  
416 respectively; considering that  $\alpha$  was simulated as 0 when the estimated  $\alpha < 0$ ,  
417 and as 2 when the estimated  $\alpha > 2$ .

418



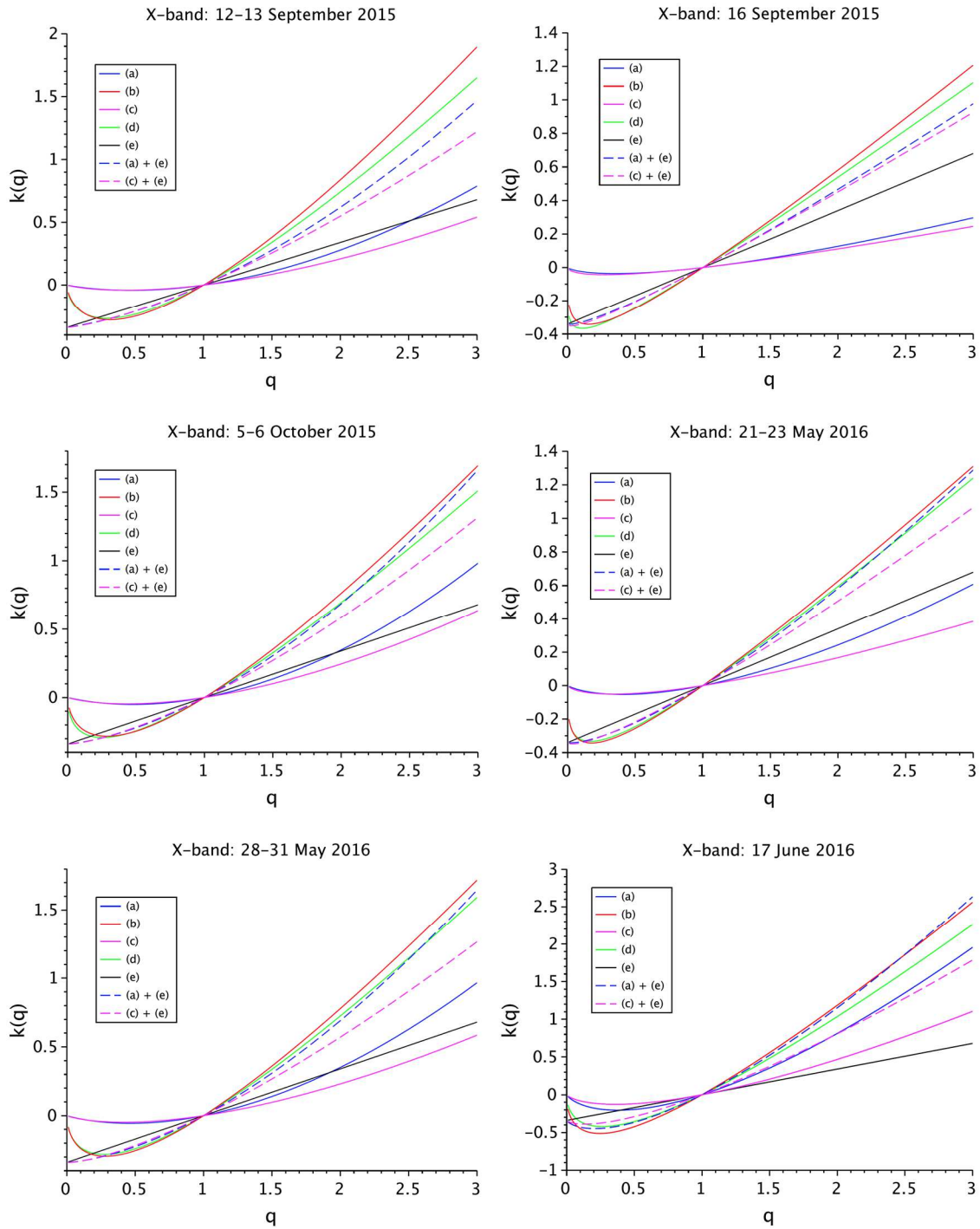


419

420

Figure 6:  $K(q)$  relations at small scales for the six studied events.

421



422

423

Figure 7:  $K(q)$  relations at large scales for the six studied events.

424

425 From Figure 6 one may note that the monofractality of fields (b) and (d)

426 at small scales (denoted by the estimated  $\alpha$  values close to 0 in Tables 2 and 4,

427 respectively) affects the suitability of the Intersection Theorem (see Section 3

428 and Eq. (23)). On the other hand, for the large scales in Figure 7 the theoretical  
 429 expression given by Eq. (23) works better for some of the events than for  
 430 others: the  $K_{(a)}(q) + K_{(e)}(q)$  curves fit better the  $K_{(b)}(q)$  ones for 05-  
 431 06/10/2015, 21-23/05/2016, 28-31/05/2016 and 17/06/2016 events than those  
 432 for 12-13/09/2015 and 16/09/2015 events. This could be easily understood by  
 433 evaluating the linear term of the Eq. (23). Indeed, the scaling moment function  
 434 of the network will correspond to the  $\beta$ -model, using Eq. (4):

$$K_{(e)}(q) = c(q - 1) \tag{24}$$

435  
 436 where over the large scales:  $c = 2 - 1.66 = 0.34$ , and this is independently  
 437 either of rainfall events, or rainfall fields.

438 Then:

$$K_{(b)}(q) = \frac{C_1}{\alpha - 1}(q^\alpha - q) + c(q - 1) = \frac{C_1}{\alpha - 1}q^\alpha - \left(\frac{C_1}{\alpha - 1} - c\right)q - c \tag{25}$$

439  
 440 The resulting scaling moment function is no longer UM function, but still  
 441 could be well approximated by it, at least between statistical moments of the  
 442 orders 1-3, when the pre-factor  $\left(\frac{C_1}{\alpha - 1} - c\right)$  of the linear term remains positive.  
 443 With  $c = 0.34$  and UM parameters from Tables 1 and 3 over large scales one  
 444 may obtain the following estimates (Tab. 5) of these pre-factors for conditions  
 445 (a) and (c):

446

Events	Rainfall field (a)	Rainfall field (c)

12-13/09/2015	-0.139	-0.01
16/09/2015	-1.545	-0.571
05-06/10/2015	-0.096	0.021
21-23/05/2016	0.325	-1.154
28-31/05/2016	-0.041	0.141
17/06/2016	9.557	-11.34

447 *Table 5: Estimated pre-factors over large scales for rainfall fields in conditions (a) and (c).*

448 Finally, the results from the multifractal analyses presented in this section  
 449 indicate a twofold discussion: (i) the events with stronger negative values of the  
 450 pre-factor give less empirical agreement with the theoretical expression of Eq.  
 451 (23); (ii) and, on the contrary, a larger positive pre-factor leads to a much  
 452 stronger convergence between the theoretical and empirical curves.

453

## 454 **5. Conclusions**

455 In this study we performed (multi)fractal analysis on rain gauge network  
 456 and X-band radar rainfall data in the context of (urban) hydrological modelling.  
 457 The main objectives of this work are to analyse the impacts of the rainfall data  
 458 spatio-temporal variability on hydrological modelling, presenting the limitations  
 459 of sparse rain gauge networks compared to high-resolution radar data, and to  
 460 discuss the suitability of radar-rain gauge conditioning considering the fractality  
 461 of rain gauge networks.

462 This paper takes the the Bièvre catchment, which is a semi-urbanised  
 463 area of 110 km<sup>2</sup> located in the southwest of Paris region, as a case study. In  
 464 this work, we used the semi-distributed modelling distribution of this area  
 465 performed with the InfoWorks CS and considered a virtual rain gauge in the  
 466 centre of mass of each sub-catchment. Then, we compared the rainfall data

467 distributions of the virtual rain gauge network with those obtained from the  
468 ENPC dual-polarised X-band radar. Firstly, we performed a fractal analysis of  
469 the virtual rain gauge network distribution and identified a scaling break at 2 km.  
470 Then we took advantage of the Intersection Theorem associated to the  
471 multifractal theory to analyse the relationship between both rain gauge and  
472 radar data.

473         The obtained results suggest that the semi-distributed hydrological  
474 models statistically reduce the rainfall fields into rainfall measured by a much  
475 scarcer network of virtual rain gauges and that inhomogeneous distributions of  
476 rain gauging networks lead to only partial information on the rainfall fields. A  
477 scaling break is retrieved in the fractal analysis of the virtual rain gauge  
478 distribution at the scale of 2 km, which is close to the average sub-catchment's  
479 size. The fractality of the rainfall support (here represented by the fixed number  
480 of 15 virtual rain gauges over the selected 8 km x 8 km area) is biased by this  
481 distribution, where the small-scale behaviour is clearly different of the large-  
482 scale one. This implies that, to respect the rainfall support fractality and its  
483 capability to consider the rainfall variability over the small scales, the same  
484 fractality of the large scales should be found at the small scales. In fact, the  
485 statistics of measured rainfall are strongly biased by the fractality of the  
486 measuring networks. This fractality needs to be properly taken into account to  
487 retrieve the original properties of the rainfall fields, in spite of the radar data  
488 calibration.

489         Additionally, a proper rainfall data re-normalisation is needed when  
490 comparing gauged rainfall with the radar data, and consequently when  
491 quantifying the impacts of space-time variability within hydrological modelling.

492 One may also note that a conditioning by the rain gauges could be rather  
493 counterproductive for rainfall events with  $\frac{C_1}{\alpha-1}$  being weaker than the  
494 codimension of the fractal rain gauge networks.

495 Furthermore, since the Bièvre catchment was calibrated to C-band radar  
496 data, in case of the number and distribution of the virtual rain gauges would be  
497 reliable in comparison to the C-band radar resolution (1 km<sup>2</sup>) – actually the  
498 SIAVB network has only 6 rain gauges –, the number of rain gauges to perform  
499 the calibration of better-resolution radar data (e.g. non polarimetric X-band  
500 radar) should be big enough to respect the same fractality of the big scales.  
501 This also means that the size of the sub-catchments should be comparable to  
502 the resolution of the rainfall data used, which would drastically increase the  
503 number of sub-catchments and become unmanageable.

504

505

506 **Funding:** This research was partially funded by the Chair “Hydrology for  
507 Resilient Cities” endowed by Veolia, and by the Department of Science and  
508 Technology of the Brazilian Army.

509

510 **Acknowledgments:** The authors greatly acknowledge partial financial supports  
511 of the Chair “Hydrology for resilient cities” endowed by Veolia, and of the  
512 Department of Science and Technology of the Brazilian Army. We would also  
513 like to thank Veolia for providing access to the hydrological model.

514

515 **Declarations of Interest:** The authors declare no conflict of interest. The  
516 funders had no role in the design of the study; in the collection, analyses, or

517 interpretation of data; in the writing of the manuscript, or in the decision to  
518 publish the results.

519

520 **Credit Author Statement:** Igor Paz: Formal analysis, Investigation,  
521 Methodology, Software, Validation, Visualization, Roles/Writing - original draft,  
522 Writing - review & editing; Ioulia Tchiguirinskaia: Conceptualization, Formal  
523 analysis, Funding acquisition, Investigation, Methodology, Project  
524 administration, Resources, Supervision, Writing - review & editing; Daniel  
525 Schertzer: Conceptualization, Formal analysis, Funding acquisition,  
526 Investigation, Methodology, Project administration, Resources, Supervision,  
527 Writing - review & editing.

528

## 529 **References**

530

531 Allegretti, M., Bertoldo, S., Prato, A., Lucianaz, C., Rorato, O., Notarpietro, R., Gabella,  
532 M., 2012. X-Band Mini Radar for Observing and Monitoring Rainfall Events.  
533 Atmospheric and Climate Sciences, 2, 290–297,  
534 <http://dx.doi.org/10.4236/acs.2012.23026>.

535

536 Alves de Souza, B., da Silva Rocha Paz, I., Ichiba, A., Willinger, B., Gires, A., Amorim,  
537 J.C.C., de Miranda Reis, M., Tisserand, B., Tchiguirinskaia, I., Schertzer, D., 2018.  
538 Multi-hydro hydrological modelling of a complex peri-urban catchment with storage  
539 basins comparing C-band and X-band radar rainfall data. Hydrological Sciences  
540 Journal, 63 (11), 1619–1635, doi.org/10.1080/02626667.2018.1520390.

541

542 Arnone, E., Pumo, D., Francipane, A., La Loggia, G., Noto, L.V., 2018. The role of  
543 urban growth, climate change, and their interplay in altering runoff extremes.  
544 Hydrological Processes, 32, 1755-1770, <https://doi.org/10.1002/hyp.13141>.  
545

546 Austin, P.M., 1987. Relationship between measured radar reflectivity and surface  
547 rainfall. Mon. Weather Rev., 115, 1053-1070, doi:10.1175/1520-  
548 0493(1987)115<1053:RBMRRRA>2.0.CO;2.  
549

550 Berne, A., Delrieu, G., Creutin, J.-D., Obled, C., 2004. Temporal and spatial resolution  
551 of rainfall measurements required for urban hydrology. J. Hydrol., 299 (3), 166–179,  
552 doi.org/10.1016/j.jhydrol.2004.08.002.  
553

554 Bringi, V.N., Chandrasekar, V., 2001. Polarimetric Doppler Weather Radar: Principles  
555 and Applications, Cambridge, Cambridge University Press.  
556

557 Chandrasekar, V., Baldini, L., Bharadwaj, N., Smith, P.L., 2015. Calibration procedures  
558 for global precipitation-measurement ground-validation radars. URSI Radio Science  
559 Bulletin, 88, 4, doi.org/10.23919/URSIRSB.2015.7909473.  
560

561 de Lima, M.I.P., Grasman, J., 1999. Multifractal analysis of 15-min and daily rainfall  
562 from a semi-arid region in Portugal. J. Hydrol., 220 (1-2), 1–11, doi.org/10.1016/S0022-  
563 1694(99)00053-0.  
564

565 Deidda, R., 2000. Rainfall downscaling in a space-time multifractal framework. Water  
566 Resour. Res., 36, 1779–1794, doi.org/10.1029/2000WR900038.  
567



568 Einfalt, T., Arnbjerg-Nielsen, K., Golz, C., Jensen, N.-E., Quirmbach, M., Vaes, G.,  
569 Vieux, B., 2004. Towards a roadmap for use of radar rainfall data in urban drainage. *J.*  
570 *Hydrol.*, 299, 186–202, doi:10.1016/j.jhydrol.2004.08.004.  
571  
572 Einfalt, T., Jessen, M., Mehlig, B., 2005. Comparison of radar and raingauge  
573 measurements during heavy rainfall. *Water Science & Technology*, 51(2), 195-201,  
574 <https://doi.org/10.2166/wst.2005.0048>.  
575  
576 Fabry, F., Bellon, A., Duncan, M.R., Austin, G.L., 1994. High resolution rainfall  
577 measurements by radar for very small basins: the sampling problem reexamined. *J.*  
578 *Hydrol.*, 161 (1-4), 415–428, [http://dx.doi.org/10.1016/0022-1694\(94\)90138-4](http://dx.doi.org/10.1016/0022-1694(94)90138-4).  
579  
580 Falconer, K., 1990. *Fractal geometry: mathematical foundations and applications*.  
581  
582 Feder, J., 1988. *Fractals (physics of solids and liquids)*. Plenum, New York.  
583  
584 Fewtrell, T.J., Duncan, A., Sampson, C.C., Neal, J.C., Bates, P.D., 2011.  
585 Benchmarking urban flood models of varying complexity and scale using high  
586 resolution terrestrial LiDAR data. *Phys. Chem. Earth, Parts A/B/C*, 36 (7–8), 281–291,  
587 [doi.org/10.1016/j.pce.2010.12.011](https://doi.org/10.1016/j.pce.2010.12.011).  
588  
589 Figueras i Ventura, J., Boumahmoud, A.-A., Fradon, B., Dupuy, P., Tabary, P., 2012.  
590 Long-term monitoring of French polarimetric radar data quality and evaluation of  
591 several polarimetric quantitative precipitation estimators in ideal conditions for  
592 operational implementation at C-band. *Q. J. R. Meteorol. Soc.*, 138, 2212–2228,  
593 doi:10.1002/qj.1934.  
594

595 Furusho, C., Andrieu, H., Chancibault, K., 2014. Analysis of the hydrological behaviour  
596 of an urbanizing basin. *Hydrol. Process.*, 28, 1809–1819, doi: 10.1002/hyp.9706.  
597

598 García-Marín, A.P., Jiménez-Hornero, F.J., Ayuso-Muñoz, J.L., 2008. Universal  
599 multifractal description of an hourly rainfall time series from a location in southern  
600 Spain. *Atmósfera*, 21(4), 347–55.  
601

602 Gires, A., Abbes, J.-B., da Silva Rocha Paz, I., Tchiguirinskaia, I., Schertzer, D., 2018.  
603 Multifractal characterisation of a simulated surface flow: a case study with Multi-Hydro  
604 in Jouy-en-Josas, France. *Journal of Hydrology*, 558, 482–495,  
605 <https://doi.org/10.1016/j.jhydrol.2018.01.062>.  
606

607 Gires, A., Tchiguirinskaia, I., Schertzer, D., Ochoa-Rodriguez, S., Willems, P., Ichiba,  
608 A., Wang, L.-P., Pina, R., Van Assel, J., Bruni, G., Tuyls, D.M., ten Veldhuis, M.-C.,  
609 2017. Fractal analysis of urban catchments and their representation in semi-distributed  
610 models: imperviousness and sewer system. *Hydrol. Earth Syst. Sci.*, 21, 2361–2375,  
611 doi:10.5194/hess-21-2361-2017.  
612

613 Grassberger, P., 1983. Generalized dimensions of strange attractors. *Physics Letters*  
614 *A*, 97(6) :227–230.  
615

616 Hentschel, H., Procaccia, I., 1983. The infinite number of generalized dimensions of  
617 fractals and strange attractors. *Physica D: Nonlinear Phenomena*, 8(3):435–444.  
618

619 Hoang, C.T., 2011. Prise en compte des fluctuations spatio-temporelles pluies-débits  
620 pour une meilleure gestion de la ressource en eau et une meilleure évaluation des  
621 risques. Ph.D. thesis, Université Paris-Est, France.  
622

623 Ichiba, A., 2016. X-band radar data and predictive management in urban hydrology.  
624 Ph.D. thesis, Earth Sciences, Université Paris-Est, France.  
625

626 Illingworth, A.J., Blackman, T.M., 2002. The need to represent raindrop size spectra as  
627 normalized gamma distributions for the interpretation of polarization radar  
628 observations. *Journal of Applied Meteorology*, 41 (3), 286–297,  
629 [https://doi.org/10.1175/1520-0450\(2002\)041<0286:TNTRRS>2.0.CO;2](https://doi.org/10.1175/1520-0450(2002)041<0286:TNTRRS>2.0.CO;2).  
630

631 Ladoy, P., Schmitt, F., Schertzer, D., Lovejoy, S., 1993. Variabilité temporelle  
632 multifractale des observations pluviométriques à Nîmes. *C. R. Acad. Sci. II*, 317, 775–  
633 782.  
634

635 Lavallée, D., Lovejoy, S., Schertzer, D., Ladoy, P., 1993. Nonlinear variability and  
636 landscape topography: analysis and simulation. *Fractals in geography*, pp. 158–192.  
637

638 Lo Conti, F., Francipane, A., Pumo, D., Noto, L. V., 2015. Exploring single polarization  
639 X-band weather radar potentials for local meteorological and hydrological applications.  
640 *Journal of Hydrology*, 531, 508–522, <https://doi.org/10.1016/j.jhydrol.2015.10.071>.  
641

642 Lovejoy, S., Schertzer, D., Tsonis, A., 1987. Functional box-counting and multiple  
643 elliptical dimensions in rain. *Science*, 235(4792):1036–1038.  
644

645 Mandelbrot, B.B. 1967. How long is the coast of Britain. *Science*, 156(3775):636–638.  
646

647 Mandelbrot, B.B., 1974. Intermittent turbulence in self-similar cascades: divergence of  
648 high moments and dimension of the carrier. *Journal of Fluid Mechanics*, 62(2):331–  
649 358.  
650

651 Mandelbrot, B.B., 1977. Fractals: form, chance and dimension.  
652  
653 Mandelbrot, B.B., Pignoni, R., 1983. The fractal geometry of nature.  
654  
655 Marshall, J.S., Palmer, W.M.K, 1948. The distribution of raindrops with size. Journal of  
656 Meteorology, 5, 165–166.  
657  
658 National Research Council of the National Academies. Urban Meteorology:  
659 Forecasting, Monitoring, and Meeting Users' Need; National Academy Press:  
660 Washington, WA, USA, 2012.  
661  
662 Ochoa-Rodriguez, S., Wang , L.-P., Gires, A., Pina, R., Reinoso-Rondinel, R., Bruni,  
663 G., Ichiba, A., Gaitan, S., Cristiano, E., van Assel, J., Kroll, S., Murlà-Tuyls, D.,  
664 Tisserand, B., Schertzer, D., Tchiguirinskaia, I., Onof, C., Willems, P., ten Veldhuis, M.-  
665 C., 2015. Impact of spatial and temporal resolution of rainfall inputs on urban  
666 hydrodynamic modelling outputs: A multi-catchment investigation. J. Hydrol., 531, 389–  
667 407, doi.org/10.1016/j.jhydrol.2015.05.035.  
668  
669 Olsson, J., Niemczynowicz, J., 1996. Multifractal analysis of daily spatial rainfall  
670 distributions. J. Hydrol., 187, 29–43, doi.org/10.1016/S0022-1694(96)03085-5.  
671  
672 Parisi, G. and Frisch, U., 1985. A multifractal model of intermittency. Turbulence and  
673 predictability in geophysical fluid dynamics and climate dynamics, pp. 84–88.  
674  
675 Paz, I.S.R., 2018. Quantifying the rain heterogeneity by X-band radar measurements  
676 for improving flood forecasting. Ph.D. thesis, Université Paris-Est, France.  
677

678 Paz, I., Willinger, B., Gires, A., Ichiba, A., Monier, L., Zobrist, C., Tisserand, B.,  
679 Tchiguirinskaia, I., Schertzer, D., 2018. Multifractal Comparison of Reflectivity and  
680 Polarimetric Rainfall Data from C-and X-Band Radars and Respective Hydrological  
681 Responses of a Complex Catchment Model. *Water*, 10 (3), 269,  
682 doi:10.3390/w10030269.

683

684 Paz, I., Willinger, B., Gires, A., Alves de Souza, B., Monier, L., Cardinal, H., Tisserand,  
685 B., Tchiguirinskaia, I., Schertzer, D., 2019. Small-Scale Rainfall Variability Impacts  
686 Analyzed by Fully-Distributed Model Using C-Band and X-Band Radar Data. *Water*, 11  
687 (6), 1273, doi:10.3390/w11061273.

688

689 Peleg, N., Ben-Asher, M., Morin, E., 2013. Radar subpixel-scale rainfall variability and  
690 uncertainty: lesson learned from observations of a dense rain-gauge network. *Hydrol.*  
691 *Earth Syst. Sci.*, 17, 2195-2208, doi:10.5194/hess-17-2195-2013.

692

693 Pina, R., Ochoa-Rodríguez, S., Simões, N., Mijic, A., Sa Marques, A., Maksimovič, C.,  
694 2016. Semi-distributed or fully distributed rainfall-runoff models for urban pluvial flood  
695 modelling? *Water*, 8 (2), 58, doi:10.3390/w8020058.

696

697 Pumo, D., Arnone, E., Francipane, A., Caracciolo, D., Noto, L.V., 2017. Potential  
698 implications of climate change and urbanization on watershed hydrology. *Journal of*  
699 *Hydrology*, 554, 80-99, <http://dx.doi.org/10.1016/j.jhydrol.2017.09.002>.

700

701 Schertzer, D. and Lovejoy, S., 1984. On the dimension of atmospheric motions.  
702 *Turbulence and Chaotic phenomena in Fluids*, pp. 505–512.

703

704 Schertzer, D. and Lovejoy, S., 1987. Physical modeling and analysis of rain and clouds  
705 by anisotropic scaling multiplicative processes. *Journal of Geophysical Research:*  
706 *Atmospheres*, 92(D8):9693–9714.

707

708 Schertzer, D. and Lovejoy, S., 1991. Nonlinear variability in geophysics.

709

710 Schertzer, D. and Lovejoy, S., 1997. Universal multifractals do exist!: Comments on “a  
711 statistical analysis of mesoscale rainfall as a random cascade”. *Journal of Applied*  
712 *Meteorology*, 36(9):1296–1303.

713

714 Schertzer, D. and Lovejoy, S., 2011. Multifractals and predictability in geophysics:  
715 chaos and multifractal insights. *The State of the Planet: Frontiers and Challenges in*  
716 *Geophysics*, pp. 317–334.

717

718 Schilling, W., 1991. Rainfall data for urban hydrology: what do we need? *Atmos. Res.*,  
719 27, 5–21, doi:10.1016/0169-8095(91)90003-F.

720

721 Seed, A., Austin, G.L., 1990. Variability of Summer Florida Rainfall and its Significance  
722 for the Estimation of Rainfall by Gages, Radar, and Satellite. *Journal of Geophysical*  
723 *Research*, 90, D3, 2207-2215, <https://doi.org/10.1029/JD095iD03p02207>.

724

725 Segond, M.L., Neokleous, N., Makropoulos, C., Onof, C., Maksimović, Č., 2007.  
726 Simulation and spatio-temporal disaggregation of multi-site rainfall data for urban  
727 drainage applications. *Hydrol. Sci. J. – J. Des Sci. Hydrol.*, 52 (5), 917–935,  
728 <http://dx.doi.org/10.1623/hysj.52.5.917>.

729

730 Selex, 2015. *Selex METEOR Manual*. Selex: Rome, Italy.

731

732 Serinaldi, F., 2010. Multifractality, imperfect scaling and hydrological properties of  
733 rainfall time series simulated by continuous universal multifractal and discrete random  
734 cascade models. *Nonlin. Processes Geophys.*, 17, 697–714, doi:10.5194/npg-17-697-  
735 2010.

736

737 Soft, M., 2010. Infoworks CS 11.0 help file. Wallingford, UK.

738

739 Tessier, Y., Lovejoy, S., Schertzer, D., 1993. Universal multifractals in rain and clouds:  
740 Theory and observations. *J. Appl. Meteorol.*, 32 (2), 223–250,  
741 [https://doi.org/10.1175/1520-0450\(1993\)032<0223:UMTAOF>2.0.CO;2](https://doi.org/10.1175/1520-0450(1993)032<0223:UMTAOF>2.0.CO;2).

742

743 Thorndahl, S., Einfalt, T., Willems, P., Nielsen, J.E., ten Veldhuis, M.-C., Arnbjerg-  
744 Nielsen, K., Rasmussen, M.R., Molnar, P., 2017. Weather radar rainfall data in urban  
745 hydrology. *Hydrol. Earth Syst. Sci.*, 21, 1359–1380, doi:10.5194/hess-21-1359-2017.

746

747 Veneziano, D., Langousis, A., Furcolo, P., 2006 Multifractality and rainfall extremes: A  
748 review. *Water Resour. Res.*, 42, W06D15, doi:10.1029/2005WR004716.

749

750 Vieux, B.E., Vieux, J.E., 2005. Statistical evaluation of a radar rainfall system for sewer  
751 system management. *Atmospheric Research*, 77, 1-4, 322-336,  
752 <https://doi.org/10.1016/j.atmosres.2004.10.032>.

753

754 Villarini, G., Mandapaka, P. V., Krrajewski, W. F., Moore, R. J., 2008. Rainfall and  
755 sampling uncertainties: A rain gauge perspective. *J. Geophys. Res. Atmos.*, 113,  
756 D11102, doi:10.1029/2007JD009214.

757

758 WMO, 2014. Guide to meteorological instruments and methods of observation. WMO-  
759 No. 8. Available online: <http://www.wmo.int/pages/prog/www/IMOP/CIMO-Guide.html>  
760 (Accessed on 14 July 2018).  
761